FERMILAB-PUB-17-374-TD

Mechanical Design Analysis of MQXFB, the 7.2 m Long Low-β Quadrupole for the High-Luminosity LHC Upgrade

G. Vallone, G. Ambrosio, N. Bourcey, D. W. Cheng, P. Ferracin, P. Grosclaude, M. Guinchard, S. Izquierdo Bermudez, M. Juchno, F. Lackner, H. Pan, J.C. Perez, S. Prestemon

***Abstract*—As part of the High-Luminosity LHC project, a set of Nb_3Sn quadrupoles are being developed aiming to enhance the performance of the inner triplets. The new magnets, identified as MQXFA and MQXFB, will share the same cross section with two different lengths, respectively 4.2 m and 7.2 m. During the magnet development, three short models were tested, along with a number of mechanical models, demonstrating the capability of the magnet cross-section to achieve the specified performances. The same performances are now required for the full-length magnets. To ensure this, the authors studied the impact of the magnet length on the capability of the structure to provide an adequate support to the coils. FE and simplified analytical models were used to evaluate the impact of the magnet length on the stresses in the magnet ends and coil elongation during powering. The models were calibrated using the results from the short model tests, and used to provide an indication on the required prestress and its foreseen impact on the magnet performance.**

***Index Terms*—High Luminosity LHC, Low-β quadrupole, Nb_3Sn magnet, Mechanical Performance.**

I. Introduction

The LHC High-Luminosity upgrade aims to reach 3000 fb^{-1} [1]. To achieve this ambitious goal the inner triplet quadrupoles, Q1, Q2 and Q3, will be upgraded with Nb_3Sn magnets. The new magnets will produce a gradient of $132.6\,\mathrm{T/m}$ with a conductor peak field of $11.4\,\mathrm{T}$. Two magnets with a magnetic length of 4.2 m, called MQXFA, will be installed in the same cryostat for the Q1 and Q3 quadrupoles. The Q2 quadrupoles (Q2a and Q2b) will be instead substituted by two magnets with a magnetic length of $7.15\,\mathrm{m}$, called MQXFB. Both designs will share the same cross-section [2]. The performance of this design was tested with three short models, produced by CERN and LARP (U.S. LHC Accelerator Research Program), sharing the MQXFB cross-section but with a magnetic length of $1.2\,\mathrm{m}$. The tests demonstrated the design capability to reach the desired performances [3]–[5].

Automatically generated dates of receipt and acceptance will be placed here
This work was supported by the High Luminosity LHC Project at CERN and by the DOE through the U.S. LHC Accelerator Research Program.

G. Vallone, N. Bourcey, P. Ferracin, P. Grosclaude, M. Guinchard, S. Izquierdo Bermudez, F. Lackner and J.C. Perez are with the European Organization for Nuclear Research (CERN), 1211 Geneva, Switzerland (e-mail: giorgio.vallone@cern.ch).

G. Ambrosio is with the Fermi National Accelerator Laboratory, Batavia, IL 80510 USA.

E. Anderssen, D. W. Cheng, M. Juchno and S. Prestemon are with Lawrence Berkeley National Laboratory, Berkeley, CA 94720 USA.

Colour versions of one or more of the figures in this paper are available online at http://ieeexplore.ieee.org.

Digital Object Identifier: xx

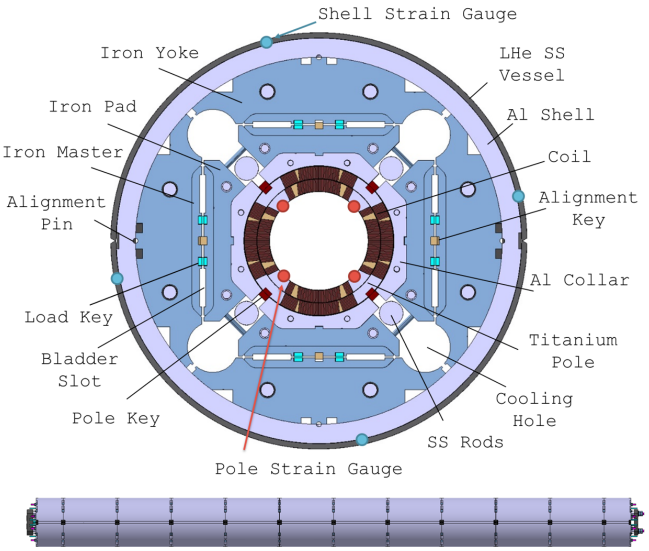

Fig. 1. MQXFB magnet design: on top, the magnet cross-section, on the bottom, a longitudinal view, showing the partitioning strategy used for the aluminum shells.

Here, we analyze the mechanical design of the MQXFB magnet, highlighting the expected differences with the short models and discussing the preload conditions required to guarantee a correct mechanical behavior.

II. MQXFB Mechanical Design

The MQXF cross-section, shown in Fig. 1, is designed to provide the azimuthal prestress by means of loading keys, inserted with the support of pressurized water bladders. The prestress is further increased during the cooldown by the differential thermal contraction of the various components. The performances of this design were extensively analyzed in [6]–[8]. It was shown that, with a sufficient preload, the structure can keep the coil in compression up to the ultimate current, equal to $17.89\,\mathrm{kA}$. Also, that this prestress can be accurately modeled with numerical methods and then monitored by means of strain gauges. To distribute uniformly the prestress along the magnet length, the aluminum shell is segmented in $683\,\mathrm{mm}$ long pieces [9]. A length of $775\,\mathrm{mm}$ was used for the short models [7]. Two shells of half length are used on the magnet ends in order to improve the stress

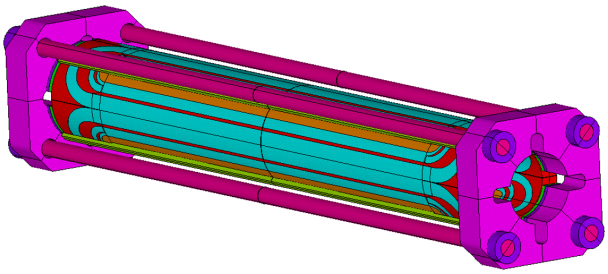

Fig. 2. MQXF longitudinal constraint configuration: the rod force is entirely transferred to the coil ends. This allows to measure the total elongation of the coil pack from the longitudinal deformation of the rods. For scale reasons, the configuration is shown on a short model coil pack.

uniformity along the magnet. The iron pads and yokes will be made of $5.8\,\mathrm{mm}$ thick laminations.

The longitudinal support system, shown in Fig. 2, is made of four rods, directly transmitting their force into the coil ends by means of a loading plate. The longitudinal prestress is applied in two steps: first, the rods are put in tension at room temperature by a piston, and blocked in position with the screw-nuts. During cool-down, the thermal contraction increases the force exerted on the coils. One of the great advantages of this configuration is the direct connection between the motion of the rod and the one of the coil ends. In fact, one can measure the longitudinal strain of the rods, and then extract the coil elongation simply multiplying the average reading to the length of the rods. The rods will be made in stainless steel, in place of the aluminum used for the short models. This change was made in an attempt to compensate for the possible decrease in longitudinal stiffness due to the magnet length.

III. Azimuthal Prestress

During the magnet powering, the electromagnetic (e.m.) forces gradually pull away the coil from the winding pole. When an insufficient prestress is applied to the magnet, the epoxy bonding may experience tension. Experiments shown that these bondings can carry only small tensions, and are then prone to break [7], [8], [10]. The consequent motions or even the energy released during the breakage are considered possible quench origins [11]–[14]. A sufficient azimuthal prestress is applied in order to avoid these effects. The MQXF design allows to control the total azimuthal prestress by varying the loading key thickness and the amount of shimming applied on the pole alignment key [8]. Numerical models and measurements from the short models suggest that a total prestress of about 140-$150\,\mathrm{MPa}$ on the winding pole is needed to keep the coil under compression.

The transfer function plot [7] in Fig. 3 describes the evolution of the pole stress as a function of the shell stress. The reference points for the computation of these stresses are the ones where the strain gauges will be installed, showed in Fig. 1. The pole stress measure is very close to the pole turn stress on the inner radius [7]. A $200\,\mu\mathrm{m}$ gap was left on the alignment key sides. This choice does not affect significantly

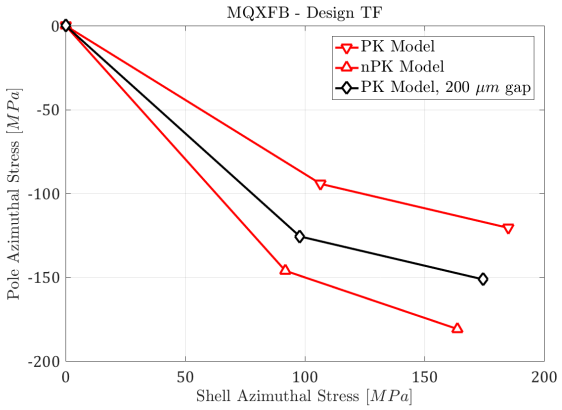

Fig. 3. Transfer Function design plot for MQXFB. The baseline case considers $200\,\mu\mathrm{m}$ of gap between the alignment pole key (PK) and the collar sides before loading at room temperature. For reference, the plot also shows the results with no gap (PK Model) and without the pole key (nPK Model).

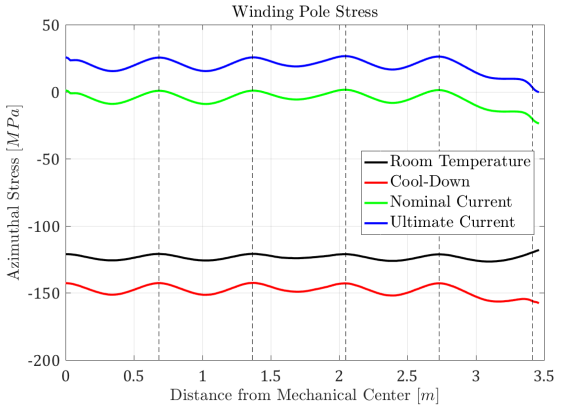

Fig. 4. Azimuthal stress on winding pole inner radius, along the magnet length. This is the same location where the strain gauges will be installed. Vertical lines show shell segmentation positions.

the field quality [15]. Results with the pole key is in contact or not with the collar sides are also provided in Fig. 3. These can be compared with the measurements to establish if the coil pack is aligned with the structure or not [7], [8].

The variation of the coil azimuthal prestress along the magnet length is shown in Fig. 4. The stress fluctuates, with minimum values in at the shell ends and maximum values at the centers. This periodic variation of the stress is narrowly contained in a $\pm 10\,\mathrm{MPa}$ range. The short model computations gave a lower range of $\pm 5\,\mathrm{MPa}$. However, this is still lower than the variability measured across the quadrants, equal to $\pm 20\,\mathrm{MPa}$ [7]. The maximum stress, equal to $-150\,\mathrm{MPa}$, becomes $-10\,\mathrm{MPa}$ at nominal current and $15\,\mathrm{MPa}$ at ultimate current. This is close to the maximum tension that was measured on the winding pole on the short models [10].

IV. Coil Ends Displacements

As in the short models, $1.2\,\mathrm{MN}$ of longitudinal electromagnetic forces are generated within the winding at the nominal current of $16.47\,\mathrm{kA}$. The forces are reacted by the coil itself, the longitudinal support system and by the structure. This last contribution is transmitted on the outer radius of the coil by

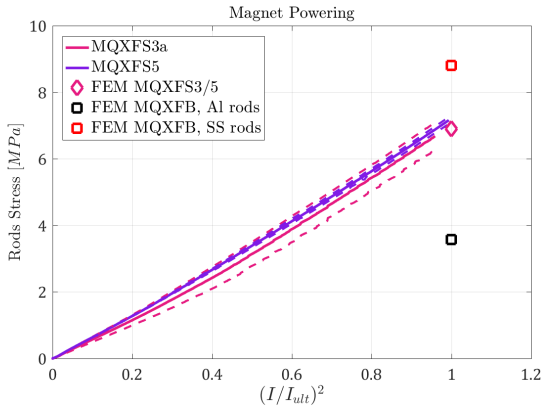

Fig. 5. Delta stress measured on the rods during powering, compared with the results from the calibrated MQXFS numerical models. The plot shows also the numerical results for MQXFB with aluminum or stainless steel rods.

TABLE I
MAIN PARAMETERS GOVERNING THE LONGITUDINAL MOTIONS

Parameter	Unit	MQXFS	MQXFB
e.m. Force, Nominal Current	MN	1.2	1.2
Coil Stiffness	MN/mm	1.10	0.17
Al. Rod Stiffness	MN/mm	0.21	0.04
SS. Rod Stiffness	MN/mm	0.53	0.14
Coil Length	m	1.08	7.00
Magnet Length	m	1.55	7.51
Coil Elongation:			
No friction, no rods	mm	1.09	7.04
No friction, Al. rods	mm	0.91	5.63
No friction, SS. rods	mm	0.73	4.22
Friction, Al. rods	mm	0.10	0.28
Friction, SS. rods	mm	0.06	0.28
Force Repartition, Coil/Rods/Structure:			
Friction, Al. rods	%	10/2/88	4/1/95
Friction, SS. rods	%	9/5/86	4/3/93

the friction with the collars, and is not negligible because of the large radial pressure.

As the coil, the rods and the structure act as a set of parallel springs, the amount of force carried by each is defined by their relative stiffness. Is then of interest to compute the coil stiffness K_{coil}. An estimate can be obtained by summing the separate contributions of its components:

$$K_{coil} = \sum E_i A_i / L \tag{1}$$

where E_i is the elastic modulus of the part, A_i its area and L the length of the straight section. The end parts contribution is neglected, since, being made mostly of stainless steel, they are much stiffer than the rest of the coil. The formula shows how the stiffness decreases linearly with the length of the magnet, justifying the swap from the aluminum rods used in the short models to the stainless steel ones. The coil and rod stiffness are reported in Table I. The table also shows how these quantities change from the short models to MQXFB. The stiffness values can be used to compute the total elongation of the coil at nominal current: when not supported by the rods or by the structure, equal to $7.04\,\mathrm{mm}$; with the rods to $4.22\,\mathrm{mm}$. In this last condition, the rods carry the 40% of the e.m. forces, while the remaining part is absorbed by the coil itself. In the short

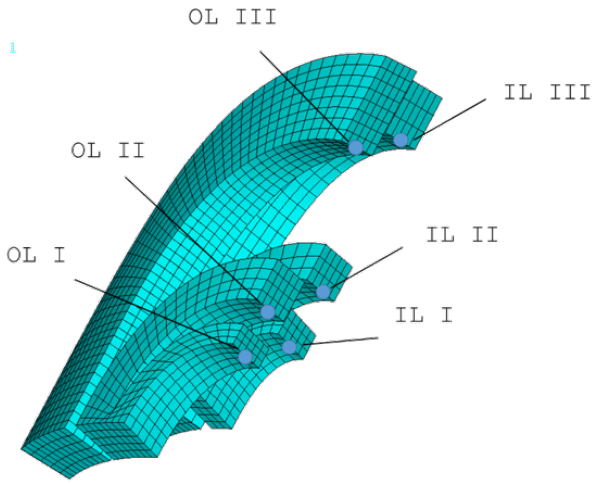

Fig. 6. Selected locations for the contact pressure analysis, shown in the meshed FEA geometry.

models the displacements with or without the aluminum rods were instead 1.09 and $0.91\,\mathrm{mm}$.

As already underlined, this model does not take into account the contact force provided by the structure. This contribution can be extracted from the rods stress measured on the short models experiments, shown in Fig. 5. The measurements were used to calibrate the numerical models, using as a fit parameter the friction coefficient between the collar and the coils. Fig. 5 shows a good agreement between the computed and measured elongation for a friction coefficient of 0.16. The model estimates a total motion of the ends equal to $0.28\,\mathrm{mm}$. The estimate for the short model was $0.10\,\mathrm{mm}$. The coil and rods stiffness from Table I can then be used to update the force distribution: the percentage of force carried by the rods becomes very small, equal to the 3% of the e.m. forces. The coil carries instead the 4%. These values do not depend on the prestress applied, as also demonstrated by the measurements shown in Fig. 5, where MQXFS3a and MQXFS5, magnets with different longitudinal prestress, share the same elongation [8].

V. CONTACT PRESSURES ON THE COIL ENDS

The magnet structure is designed to oppose the azimuthal e.m. forces and keep the coil always in compression against the winding pole [2], [16]. This condition is generally imposed to avoid a local loss of stiffness and consequent motions. In a similar fashion, one should assure the same condition in the coil end region, where the winding is compressed against the winding pole and the end-spacers.

A set of representative locations, shown in Fig. 6, was selected to verify that this condition is satisfied. The contact pressures were computed using the model calibrated on the short model experiments, considering the following cases: MQXFS3a; MQXFB with the aluminum rods producing at cold half of the e.m. forces at nominal current; MQXFB with stainless steel rods and the same stress; MQXFB with stainless steel rods producing the full nominal e.m. force at cold. The longitudinal rod stresses are reported in Table II. The results

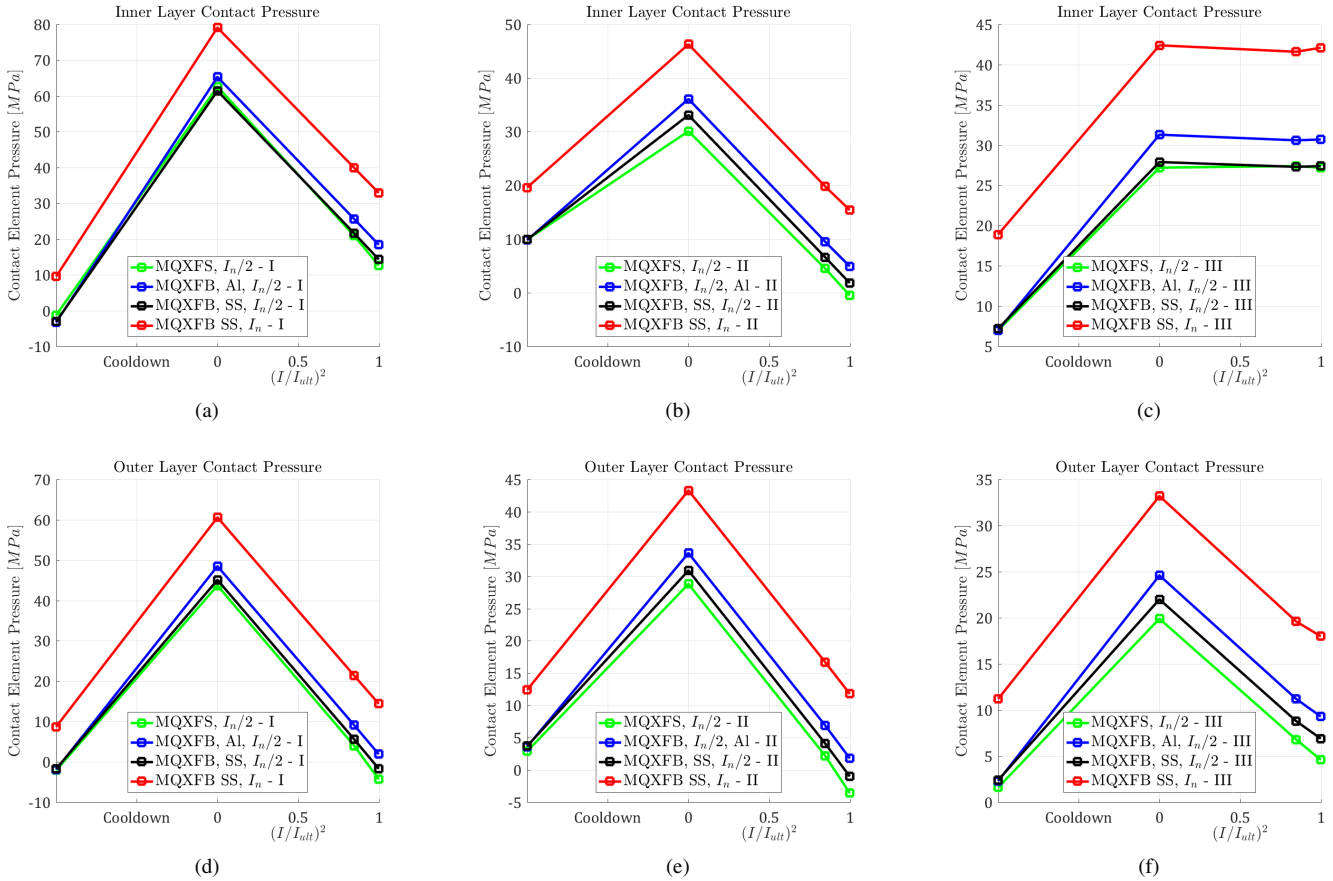

Fig. 7. Evolution of the contact pressure during magnet loading, cooldown and powering at nominal and ultimate current, computed with numerical models on the locations shown in Fig. 6. The stress on the rods is given in Table II. (a): IL, I. (b): IL, II. (c): IL, III. (d): OL, I. (e): OL, II. (f): OL, III.

TABLE II
PARAMETERS USED IN THE END-ZONE CONTACT ANALYSIS

Rods Longitudinal Stress - MPa			
	R.T.	CD	I_{ult}
MQXFS3a, $I_n/2^{\dagger}$	56	168	173
MQXFB, Al. Rods, $I_n/2$	62	219	223
MQXFB, SS Rods, $I_n/2$	64	187	196
MQXFB, SS Rods, $I_n^{\ddagger}$	174	302	311

† Rods force at cold equal to half of the e.m. force at nominal current I_n.
‡ Rods force at cold equal to the e.m. force at nominal current.

with the aluminum rods show that the prestress increase during cooldown is 40% larger in the long magnet.

The contact pressure evolution is reported in Fig. 7. The plots show the pressure values after the R.T. loading, its increase during cooldown, and the unloading due to e.m. forces. The plots also show how the rods stress increase due to the magnet length is reflected on the contact pressures. The comparison between aluminum and steel rods shows a lower increase of prestress during cooldown. The powering is not affected instead.

The most critical locations are IL II and OL I. These locations can in fact undergo tension during the powering with the lower prestress condition. But, with the higher loading condition, the curves are moved vertically, increasing the pressure at all the stages. This guarantees pressures greater then zero up to the ultimate current, in all the locations considered.

VI. Conclusion

The authors discussed the mechanical design of the MQXFB magnet. The azimuthal and longitudinal loading conditions needed to guarantee a correct operation up to ultimate current were reported.

As for the short models, an azimuthal prestress of 150 MPa on the winding pole will prevent the unloading up to ultimate current. The stress variation along the length, due to the segmented aluminum shell will be larger than the short model one but still contained in a ± 10 MPa range.

Models allowed to predict the longitudinal motions of the coil during the powering. Results show that the percentage of e.m. forces carried by the structure will be increased from the 88% of the short models to 93%. The longitudinal loading system will carry only the 3%, and the remaining 4% will be distributed in the coil. The total elongation of the coil was 0.28 mm, about three times the one of the short models. Nevertheless, computations demonstrated that the rods prestress is of foremost importance to guarantee a proper contact condition in the coil end-region.

REFERENCES

[1] L. Rossi and O. Brüning, "High Luminosity Large Hadron Collider: a description for the European Strategy Preparatory Group," CERN, Geneva, Swtizerland, CERN-ATS-2012-236, 2012.

[2] P. Ferracin *et al.*, "Development of MQXF: The Nb_3Sn low-β quadrupole for the HiLumi LHC," *IEEE Transactions on Applied Superconductivity*, vol. 26, no. 4, pp. 1–7, 2016.

[3] G. Chlachidze *et al.*, "Performance of the first short model 150-mm-aperture Nb_3Sn quadrupole MQXFS for the High-Luminosity LHC upgrade," *IEEE Transactions on Applied Superconductivity*, vol. 27, no. 4, pp. 1–5, Jun. 2017.

[4] S. Stoynev *et al.*, "Summary of test results of MQXFS1 - the first short model 150 mm aperture Nb_3Sn quadrupole for the High-Luminosity LHC upgrade," *IEEE Transactions on Applied Superconductivity*, 2017, Under Review.

[5] H. Bajas *et al.*, "Test results of the short models MQXFS3 and MQXFS5 for the HL-LHC upgrade," *IEEE Transactions on Applied Superconductivity*, 2017, Under Review.

[6] M. Juchno *et al.*, "Mechanical qualification of the support structure for MQXF, the Nb_3Sn low-β quadrupole for the high luminosity LHC," *IEEE Transactions on Applied Superconductivity*, vol. 26, no. 4, 2016.

[7] G. Vallone *et al.*, "Mechanical performance of short models for MQXF, the Nb_3Sn low-β quadrupole for the Hi-Lumi LHC," *IEEE Transactions on Applied Superconductivity*, pp. 1–5, 2016.

[8] G. Vallone *et al.*, "Mechanical analysis of the short model magnets for the Nb_3Sn low-β quadrupole MQXF," *IEEE Transactions on Applied Superconductivity*, 2017, Under Review.

[9] P. Ferracin *et al.*, "Assembly and test of a support structure for 3.6 m long Nb_3Sn racetrack coils," *IEEE Transactions on Applied Superconductivity*, vol. 18, no. 2, pp. 167–170, Jun. 2008.

[10] G. Vallone and P. Ferracin, "Modeling coil-pole debonding in Nb_3Sn superconducting magnets for particle accelerators," *IEEE Transactions on Applied Superconductivity*, 2017, Under Review.

[11] M. N. Wilson, *Superconducting magnets*. 1983.

[12] A. Devred, "Quench origins," in *AIP*, vol. 1262, 1992, pp. 1262–1308.

[13] P. Ferracin and S. Caspi, "Finite element model of training in the superconducting quadrupole magnet SQ02," *Cryogenics*, vol. 47, no. 11-12, pp. 595–606, 2007.

[14] R. Wands, "Magneto-structural analysis of the fermilab TQC Nb_3Sn high gradient quadrupole end region," *Cryogenics*, vol. 47, no. 11-12, pp. 607–617, 2007.

[15] S. Izquierdo Bermudez *et al.*, "Geometric field errors of short models for MQXF, the Nb_3Sn low-beta quadrupole for the high luminosity LHC," *IEEE Transactions on Applied Superconductivity*, 2017, Under Review.

[16] P. Ferracin *et al.*, "Magnet design of the 150 mm aperture low-β quadrupoles for the high luminosity LHC," *IEEE Transactions on Applied Superconductivity*, vol. 24, no. 3, pp. 1–6, 2014.